JOURNAL OF GEOPHYSICAL RESEARCH, VOL. 117, A07216, doi:10.1029/2012JA017827, 2012

Effects of finite plasma pressure on centrifugally driven convection in Saturn's inner magnetosphere

X. Liu[1] and T. W. Hill[1]

Received 13 April 2012; revised 6 June 2012; accepted 9 June 2012; published 21 July 2012.

[1] We have previously shown simulation results for centrifugally driven plasma convection in Saturn's inner magnetosphere ($2 < L < 12$) using the Rice Convection Model, including a continuously active distributed plasma source, and the effects of the Coriolis force and the pickup current. These simulations result in a quasi-steady state, in which fast, narrow inflow channels alternate with slower, wider outflow channels, consistent with Cassini Plasma Spectrometer observations. These previous simulations, however, did not include the plasma pressure. We investigate here the effects of finite plasma pressure and the associated gradient-curvature drift current by giving the cold plasma a finite temperature. Our simulations confirm the theoretical expectation that a finite plasma pressure produces a force in the positive radial direction, the same direction as the centrifugal force, and acts as an additional driver of plasma convection. Our simulations also confirm that the radial velocities can be reduced (to keep them within observational constraints) by increasing the assumed ionospheric Pedersen conductance (also within observational constraints).

Citation: Liu, X., and T. W. Hill (2012), Effects of finite plasma pressure on centrifugally driven convection in Saturn's inner magnetosphere, *J. Geophys. Res.*, *117*, A07216, doi:10.1029/2012JA017827.

1. Introduction

[2] Saturn's unique magnetosphere is dominated by a broadly distributed source of neutral water molecules, mainly derived from the south pole Enceladus plume and scattered by charge exchange and neutral-neutral collisions [*Johnson et al.*, 2006]. In Saturn's rotating magnetosphere, this wide neutral gas cloud produces a widely distributed plasma source which drives a centrifugally driven convection system. Since Cassini's arrival at Saturn in 2004, the Cassini Plasma Spectrometer (CAPS) [*Young et al.*, 2005] has provided observational evidence of this magnetospheric convection system. *Hill et al.* [2005] and *Chen et al.* [2010] studied the injection/dispersion signatures and found that the inflow channels occupy only a small fraction (about 5–10%) of the total longitude space. In previous work [*Liu et al.*, 2010], we used the Rice Convection Model (RCM) and included a continuously active distributed inner plasma source, and the effects of the Coriolis force and the pickup current, to simulate the plasma convection pattern. These simulations confirmed that fast, narrow inflow channels alternate with slower, wider outflow channels in Saturn's inner magnetosphere. Those simulations did not include the effects of plasma pressure, because plasma temperature was set to 0.

[3] *Wilson et al.* [2008] used CAPS data to investigate positive ion velocity moments at near-equatorial latitudes, including ion velocities, temperatures and temperature anisotropies. They reported that the temperature of magnetospheric ions increases with radial distance from Saturn, and exhibits temperature anisotropies with $T_\perp/T_\parallel$ ratios ~3–8 in Saturn's inner magnetosphere. *Wilson et al.* [2009] extended the ion azimuthal velocity profile inward to 3 Rs.

[4] The study described here extends the simulation study of plasma convection in Saturn's inner magnetosphere by including the effects of finite plasma pressure and the associated gradient-curvature drift by giving the cold plasma a finite temperature. We also investigate the effects of variations of the ionospheric Pedersen conductance.

2. Simulation Setup

2.1. Representation of Plasma Pressure

[5] We include the effects of finite plasma pressure by giving the cold plasma a finite temperature. In Saturn's inner magnetosphere, the W^+ (water group ion) temperature is anisotropic with $T_\perp/T_\parallel$ ratios ~3–8 [*Wilson et al.*, 2008]. Therefore, we consider the perpendicular temperature only. The finite perpendicular temperature produces an average force in the positive radial direction (near the equatorial plane) given by

$$\mathbf{F}_{\nabla B} = -\langle\mu\rangle\nabla B = \frac{3kT_\perp}{r_e}\hat{\mathbf{e}}_r \quad (1)$$

where $\langle\mu\rangle = kT_\perp/B$ is the average ion magnetic moment, k is Boltzmann's constant, $T_\perp$ is the W^+ perpendicular

[1]Physics and Astronomy Department, William Marshall Rice University, Houston, Texas, USA.

Corresponding author: X. Liu, Physics and Astronomy Department, William Marshall Rice University, PO Box 1892, Houston, TX 77251-1892, USA. (xareo@rice.edu)

0148-0227/12/2012JA017827

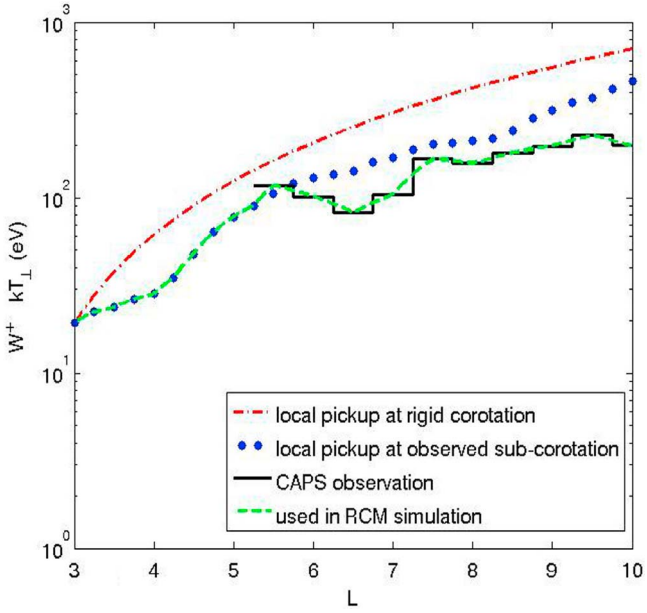

Figure 1. Water group ion (W^+) perpendicular temperatures. The dash-dotted line is appropriate to local pick-up at the rigid corotation speed, and the dotted line to local pickup at the observed sub-corotation speed [*Wilson et al.*, 2009]. The solid line is the observed perpendicular temperature [*Wilson et al.*, 2008]. The dashed line, used in the simulations, follows the dotted line in the range L = 3–5.5, and the solid line in the range L = 5.5–10.

temperature, r_e is the radial distance from Saturn's center in the equatorial plane, and the aligned dipole approximation $|\nabla B|/B = 3/r_e$ is adopted (as in previous RCM-Saturn simulations) for Saturn's magnetic field near the equatorial plane.

[6] Figure 1 shows sample radial profiles of the W^+ perpendicular temperature. The dash-dotted line is the W^+ temperature appropriate to pick up at the local rigid corotation speed. The dotted line is the W^+ temperature appropriate to local pickup at the observed sub-corotation speed [*Wilson et al.*, 2009]. The solid line is the observed W^+ perpendicular temperature where available [*Wilson et al.*, 2008]. The observed temperature (solid line) is available in the region 5.5–10 Rs, and is smaller than the temperature appropriate to local pickup at the observed sub-corotation speed (dotted line), indicating that some of the observed W^+ ions were picked up, not locally, but closer to Saturn. We assume local pickup temperatures in the closer region 3–5.5 Rs for lack of observed temperature data there. The dashed line is the W^+ temperature used in the simulation, which takes the value of temperature appropriate to local pickup at the observed sub-corotation speed (dotted line) in the region 3–5.5 Rs, and the observed temperature (solid line) in the region 5.5–10 Rs. This profile is extrapolated smoothly inward and outward, respectively, to the regions $2 < L < 3$ and $10 < L < 12$ that are included in the simulations but not in the observations.

[7] Note that this radial profile is quite different from that expected for inward compression of plasma from an exterior source (as assumed, for example, in terrestrial applications of the RCM) because most of the ions' thermal energy here derives from rotational pick-up at, or inward of, the point of observation. It would be impractical to attempt to model this heating process explicitly within the RCM simulation because it affects, and is affected by, the radial transport process that we are attempting to simulate. Instead we take the ion temperature as an empirical input in order to assess its effect on transport. The electron temperature is neglected because it is known to be much smaller than the ion temperature [cf. *Schippers et al.*, 2008; *Thomsen et al.*, 2010].

[8] For comparison, the centrifugal force near the equatorial plane is

$$\mathbf{F}_C = m\boldsymbol{\Omega}^2 r_e \hat{e}_r \tag{2}$$

where m is the average mass of W^+ ions (taken to be 17 amu for the observed mixture of O^+, OH^+, H_2O^+, and H_3O^+), and Ω is the observed angular velocity of partial corotation. With the observed temperature data in Figure 1, we can easily calculate the ratio $F_{\nabla B}/F_C$, which varies about an average value ~0.5 in the region of interest. The $-\mu\nabla B$ force is in the same direction as the centrifugal force near the equatorial plane, and of a comparable magnitude. It therefore provides an additional driver of the magnetospheric convection system.

[9] As in previous RCM simulations for Jupiter [e.g., *Wu et al.*, 2007] and for Saturn [e.g., *Liu et al.*, 2010], we represent the magnetospheric plasma sheet as an equatorially confined sheet. Also, as in all previous RCM simulations (including terrestrial ones), we represent the pressure-gradient force in terms of its associated guiding-center drift currents. In general, the pressure-gradient current is the sum of all guiding-center drift currents and the magnetization current, but the latter is identically divergence-free (being defined as the curl of the magnetization vector), so it does not contribute to the ionosphere-magnetosphere coupling currents that the RCM attempts to simulate.

2.2. Representation of Plasma Source

[10] In previous RCM-Saturn work, we used an interior plasma source based on the neutral cloud model of *Johnson et al.* [2006] (we called it the J06 source model). This source model, however, has a total mass loading rate of only about 24 kg/s [*Liu et al.*, 2010, Figure 1]. More recent plasma source models [*Smith et al.* 2010; *Cassidy and Johnson*, 2010] suggest a larger mass loading rate ~150 kg/s. Moreover, *Chen et al.* [2010] analyzed CAPS observational data and estimated a global plasma mass outflow rate ~280 kg/s from Saturn's inner magnetosphere. We therefore scale the J06 plasma source model upward by a factor 10 to ~240 kg/s to agree with present observational and model estimates. Figure 2 shows the inner source model after scaling up. Panel a shows both charge exchange rate and ionization rate per equatorial area, and panel b shows the ionization rate per equatorial area and per unit magnetic flux.

[11] We also scale the ionospheric Pedersen conductance Σ_p upward by the same factor 10 to keep the simulated radial flow speeds within the observational bounds established by *Chen et al.* [2010]. This increased value of Σ_p is in fact closer to the bounds established by the observation-based aeronomy model results of *Moore et al.* [2010]. According to equations (4)–(8) in *Liu et al.* [2010], the impact of changing the plasma source strength is counteracted by changing the

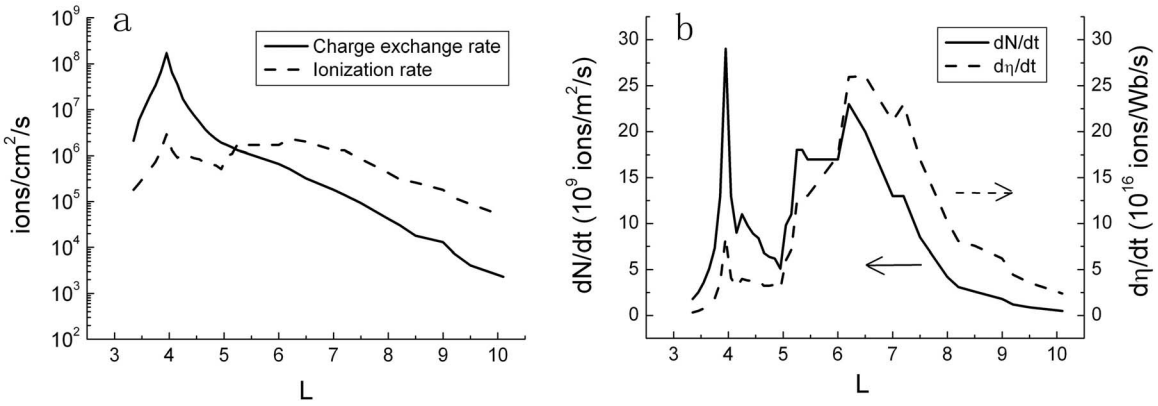

Figure 2. Interior plasma source model obtained by scaling the J06 model upward by a factor 10. (a) Charge exchange rate and ionization rate per unit equatorial area. (b) Ionization rate per unit equatorial area and per unit magnetic flux.

ionospheric Pedersen conductance in the same way. Though there are some differences in the details of the convection pattern, which includes an element of chaos, these are not large enough to change the statistical results significantly.

3. Simulation Results

[12] To illustrate the effects of finite plasma pressure, we show three sets of RCM simulation results:

[13] (A) No plasma pressure ($T_\perp = 0$; $\Sigma_p = 3$ S).

[14] (B) Finite plasma pressure ($T_\perp$ given by dashed line in Figure 1, $\Sigma_p = 3$ S).

[15] (C) Finite plasma pressure, $\Sigma_p = 6$ S.

[16] In simulations A and B, the value $\Sigma_p = 3$ S is 10 times that assumed by *Liu et al.* [2010], as discussed above. In simulation C, Σ_p is increased to 6 S to constrain the larger radial velocities caused by the inclusion of plasma pressure, as also discussed above. The value 6 S used here is well within the bounds established by the observation-based aeronomical models of *Moore et al.* [2010].

[17] Figure 3 shows all three sets of simulation results in the equatorial plane as viewed from north, in Saturn's corotating frame. The color bar shows the values of η, the plasma ion content per unit magnetic flux. We show representative snapshots at similar stages of evolution: (from top to bottom) the appearance of outflow fingers, and the developing, pre-mature, and mature fingers. The simulations begin with an empty magnetosphere. For the first few hours, the plasma accumulates in the region where the plasma source peaks. The first few hours are not shown here; they are basically the same as Figure 3a in *Liu et al.* [2010] except that the color bar is shifted by a factor 10. After sufficient accumulation time, the outflow fingers appear as a result of the centrifugal interchange instability (top row). In simulation B, the outflow fingers appear earlier than in simulation A. This confirms that the $-\mu\nabla B$ force provides an additional driving force, accelerating the evolution of the convection system. In simulation C, the outflow fingers take longer to appear, confirming that the interchange instability is suppressed by higher Pedersen conductance. Once the outflow fingers appear, the plasma accumulated in the torus (red rings) at earlier times is drained by outward motion.

[18] In the second row, the heads of the outflow fingers are broader in simulation B than those in simulations A or C. The reason may be that the larger radial velocities (shown in Figure 4) produce larger Coriolis accelerations, and thus larger azimuthal velocities. During their nonlinear growth in the third row, the outflow fingers are clearly bent in the retrograde direction by the Coriolis acceleration and the pickup effect. The bottom row shows the quasi-steady states that have been reached at the end of each simulation, in which fast, narrow inflow channels (the blue regions, almost devoid of plasma from the internal source) alternate with slower, wider outflow channels.

[19] Figure 4 shows comparisons of simulation results with CAPS observations. In each panel, the dashed line, the dash-dotted line, and the dotted line show statistical results of simulations A, B and C, respectively. Those simulation results are averaged over 1/2 h intervals during the quasi-steady state, defined as the state reached late in the simulation when the total plasma content in the region 2–12 R_S, and the radial velocities and inflow width ratios, do not change much with time in a statistical time-averaged sense. The black solid line (histogram) shows the CAPS observations reported by *Chen et al.* [2010].

[20] The top two panels show the outflow and inflow velocities, averaged over longitude within the respective outflow and inflow channels. Simulation B has larger radial velocities, both inflow and outflow, than simulation A. The obvious reason is the finite plasma pressure included in B but not A. The ratio of the radial velocities in simulation B to those in simulation A is about 1.5–1.8. This is consistent with the theoretical expectation based on the fact that the $-\mu\nabla B$ force is about 1/2 of the centrifugal force. (The convection system is nonlinear. Other factors, such as the Coriolis acceleration and the pickup current, also affect the convection pattern.) In simulation C, we impose a larger Pedersen conductance, and successfully reduce the radial velocities to within observational constraints.

[21] The middle panel shows the radial profile of the inflow longitudinal width ratio, i.e., the fraction of the 2π longitudinal space that is occupied by inflow channels. The observations [*Chen et al.*, 2010] show that the inflow injection structures occupy only about 5–10% of the longitude

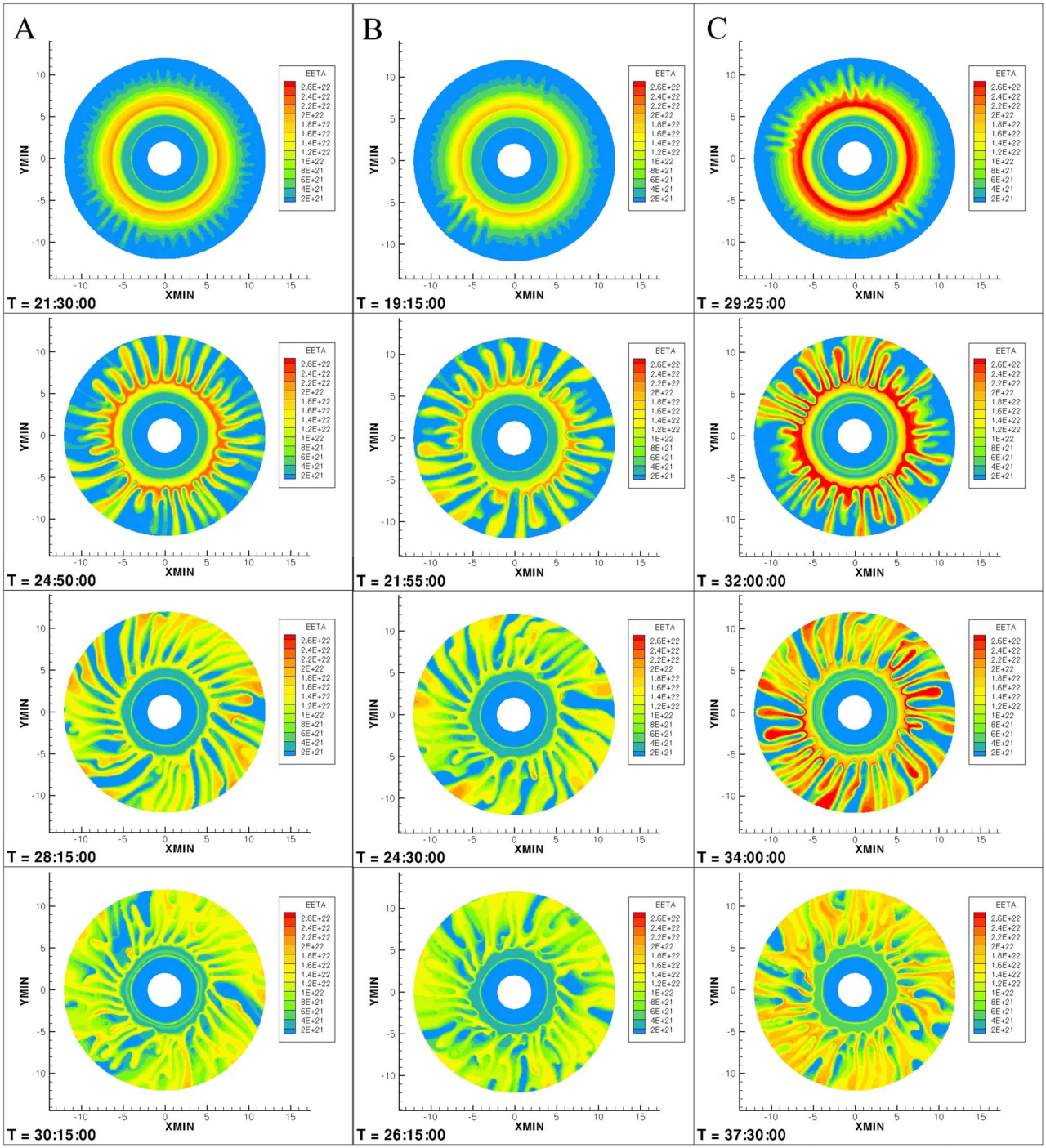

Figure 3. Evolution of plasma convection in three RCM simulations. The color bar shows plasma ion content per unit magnetic flux η in Saturn's equatorial plane, in the corotating frame. (a) No plasma pressure and $\Sigma_p = 3.0$ S. (b) Observed plasma pressure and $\Sigma_p = 3.0$ S. (c) Observed plasma pressure and $\Sigma_p = 6.0$ S. Time labels are in h:m:s.

space at a given distance, consistent with the present simulation results.

[22] The second from bottom panel shows the outflow mass transport rate. At 10 Rs, close to the outer boundary of our simulations, the outflow mass transport rates of the simulations are in the range 190–260 kg/s. These values are roughly consistent with the imposed total mass loading rate of 240 kg/s. This confirms our identification of quasi-steady states, during which the total interior plasma source rate is roughly balanced by the outflow flux. The outflow mass rate inferred from observations is slightly larger, ~280 kg/s [*Chen et al.*, 2010].

[23] The bottom panel shows the flux tube plasma mass content η, averaged over longitude. The values of η in

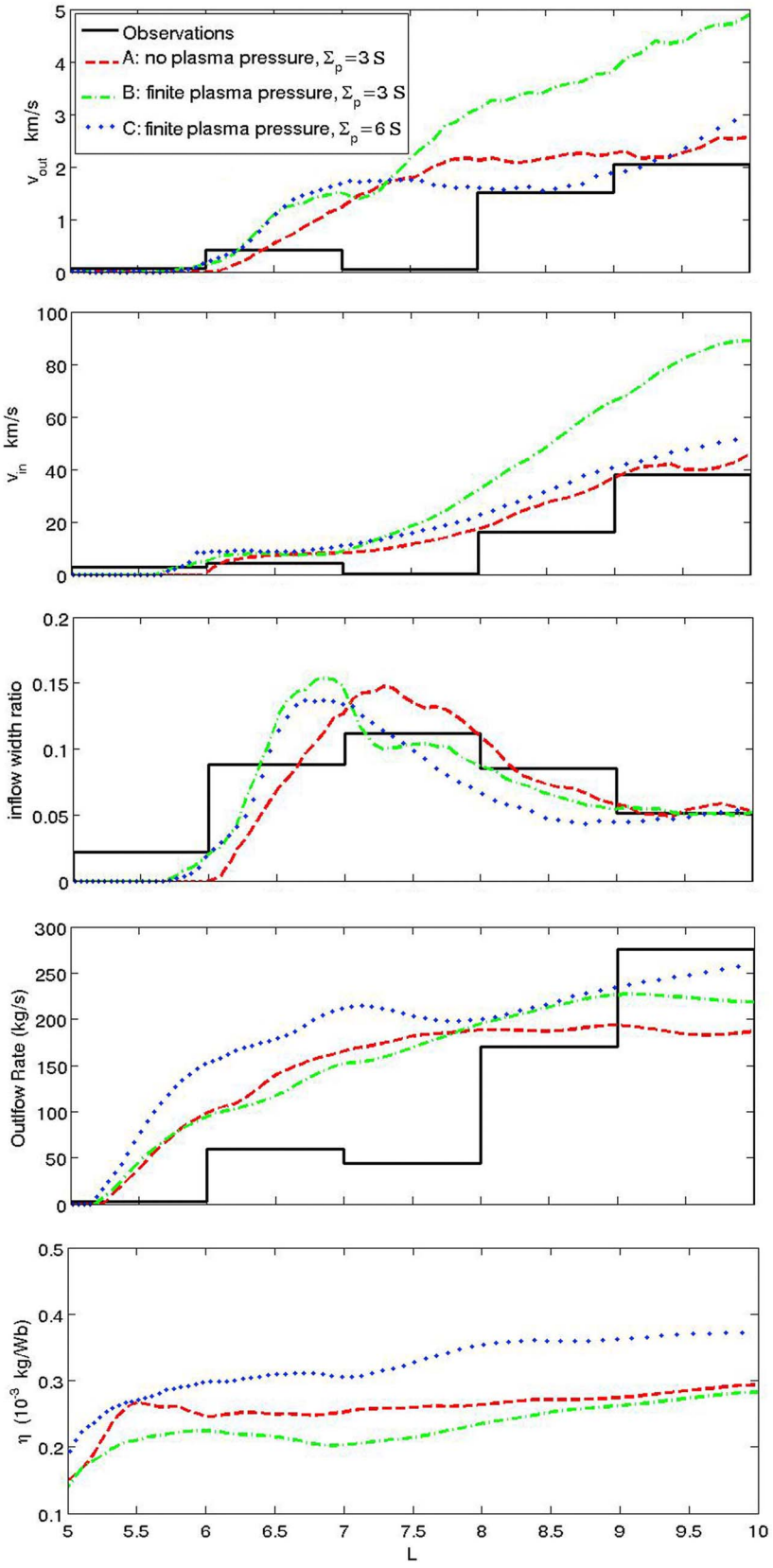

Figure 4. Comparisons between observations [*Chen et al.*, 2010] and simulation results for three RCM runs. (top to bottom) Outflow velocities v_{out}, inflow velocities v_{in}, inflow longitudinal width ratio, mass outflow rate, and flux tube plasma mass content η. The top two panels and the bottom panel are averaged over longitude.

simulation C are larger than in simulations A and B, as also shown in Figure 3. The reason is probably that the higher ionospheric Pedersen conductance in simulation C suppresses the interchange instability and confines more plasma in the simulated region. Simulations A and B have the same Pedersen conductance. Because simulation B has the extra driving force (finite plasma pressure) and correspondingly larger outflow velocities, η in simulation B is smaller than in simulation A. However, even in simulation C, η is smaller than indicated by observations [*Chen et al.*, 2010, Figure 5]. This may suggest a higher mass loading rate and a higher ionospheric Pedersen conductance.

4. Conclusions

[24] We have generalized our previous RCM-Saturn simulations [*Liu et al.*, 2010] by incorporating the effects of finite plasma pressure and the associated gradient drift current. Observations have shown, as expected, that the ion temperature is anisotropic with $T_\perp > T_\parallel$. Our simulations confirm the theoretical expectation that the finite plasma pressure provides a $-\mu\nabla B$ force in the positive radial direction, which augments the driving force provided by the centrifugal force. The magnitude of the $-\mu\nabla B$ force is about 1/2 the magnitude of the centrifugal force, and thus provides a $\sim$50% enhancement of the centrifugal instability growth rate. Our simulations also confirm that the ionospheric Pedersen conductance constrains the radial velocities of plasma flow. This is consistent with the results of earlier analytical models [e.g., *Huang and Hill*, 1991] which have, however, been restricted so far to simpler initial-value problems with no continuously active plasma source.

[25] In future work, we plan to incorporate a source of hotter but more tenuous plasma at the outer simulation boundary in an attempt to simulate the injection/dispersion signatures observed by CAPS [*Hill et al.*, 2005; *Chen et al.*, 2010].

[26] **Acknowledgments.** We thank R. J. Wilson for providing the water group ion temperature data shown in Figure 1; R. E. Johnson for providing the source model data; and S. Sazykin, R. W. Spiro, M. F. Thomsen, and R. A. Wolf for helpful discussions. This work was supported by NASA grant NNX09AH99G to Rice University and by NASA JPL contract 1243218 to the Southwest Research Institute.

[27] Masaki Fujimoto thanks the reviewers for their assistance in evaluating this paper.

References

Cassidy, T. A., and R. E. Johnson (2010), Collisional spreading of Enceladus' neutral cloud, *Icarus*, *209*, 696–703 doi:10.1016/j.icarus.2010.04.010.

Chen, Y., T. W. Hill, A. M. Rymer, and R. J. Wilson (2010), Rate of radial transport of plasma in Saturn's inner magnetosphere, *J. Geophys. Res.*, *115*, A10211, doi:10.1029/2010JA015412.

Hill, T. W., A. M. Rymer, J. L. Burch, E. J. Crary, D. T. Young, M. F. Thomsen, D. Delapp, N. André, A. J. Coates, and G. R. Lewis (2005), Evidence for rotationally driven plasma transport in Saturn's magnetosphere, *Geophys. Res. Lett.*, *32*, L14S10, doi:10.1029/2005GL022620.

Huang, T. S., and T. W. Hill (1991), Drift-wave instability in the Io plasma torus, *J. Geophys. Res.*, *96*, 14,075–14,083, doi:10.1029/91JA01170.

Johnson, R. E., H. T. Smith, O. J. Tucker, M. Liu, M. H. Burger, E. C. Sittler, and R. L. Tokar (2006), The Enceladus and OH tori at Saturn, *Astrophys. J.*, *644*, L137–L139, doi:10.1086/505750.

Liu, X., T. W. Hill, R. A. Wolf, S. Sazykin, R. W. Spiro, and H. Wu (2010), Numerical simulation of plasma transport in Saturn's inner magnetosphere using the Rice Convection Model, *J. Geophys. Res.*, *115*, A12254, doi:10.1029/2010JA015859.

Moore, L., I. Mueller-Wodarg, M. Galand, A. Kliore, and M. Mendillo (2010), Latitudinal variations in Saturn's ionosphere: Cassini measurements and model comparisons, *J. Geophys. Res.*, *115*, A11317, doi:10.1029/2010JA015692.

Schippers, P., et al. (2008), Multi-instrument analysis of electron populations in Saturn's magnetosphere, *J. Geophys. Res.*, *113*, A07208, doi:10.1029/2008JA013098.

Smith, H. T., R. E. Johnson, M. E. Perry, D. G. Mitchell, R. L. McNutt, and D. T. Young (2010), Enceladus plume variability and the neutral gas densities in Saturn's magnetosphere, *J. Geophys. Res.*, *115*, A10252, doi:10.1029/2009JA015184.

Thomsen, M. F., D. B. Reisenfeld, D. M. Delapp, R. L. Tokar, D. T. Young, F. J. Crary, E. C. Sittler, M. A. McGraw, and J. D. Williams (2010), Survey of ion plasma parameters in Saturn's magnetosphere, *J. Geophys. Res.*, *115*, A10220, doi:10.1029/2010JA015267.

Wilson, R. J., R. L. Tokar, M. G. Henderson, T. W. Hill, M. F. Thomsen, and D. H. Pontius (2008), Cassini plasma spectrometer thermal ion measurements in Saturn's inner magnetosphere, *J. Geophys. Res.*, *113*, A12218, doi:10.1029/2008JA013486.

Wilson, R. J., R. L. Tokar, and M. G. Henderson (2009), Thermal ion flow in Saturn's inner magnetosphere measured by the Cassini plasma spectrometer: A signature of the Enceladus torus, *Geophys. Res. Lett.*, *36*, L23104, doi:10.1029/2009GL040225.

Wu, H., T. W. Hill, R. A. Wolf, and R. W. Spiro (2007), Numerical simulation of fine structure in the Io plasma torus produced by the centrifugal interchange instability, *J. Geophys. Res.*, *112*, A02206, doi:10.1029/2006JA012032.

Young, D. T., et al. (2005), Composition and dynamics of plasma in Saturn's magnetosphere, *Science*, *307*, 1262–1266, doi:10.1126/science.1106151.